Development and Evaluation of a Hydrostatic Dynamical Core using the Spectral element/Discontinuous Galerkin Methods

Suk-Jin Choi[1),*] and Francis X. Giraldo[2)]

1) Korea institute of atmospheric prediction systems, 4F., 35 Boramae-ro 5-gil, Dongjak-gu, Seoul 156-849, Korea

2) Department of Applied Mathematics, Naval Postgraduate School, 833 Dyer Road, Monterey, CA 93943, USA

April, 2014,

Submitted to *Monthly Weather Review*

---

*Corresponding author address: Dr. Suk-Jin Choi, Korea institute of atmospheric prediction systems, 4F., 35 Boramae-ro 5-gil, Dongjak-gu, Seoul 156-849, Korea. Email: sj.choi@kiaps.org

Report Documentation Page

Form Approved
OMB No. 0704-0188

Public reporting burden for the collection of information is estimated to average 1 hour per response, including the time for reviewing instructions, searching existing data sources, gathering and maintaining the data needed, and completing and reviewing the collection of information. Send comments regarding this burden estimate or any other aspect of this collection of information, including suggestions for reducing this burden, to Washington Headquarters Services, Directorate for Information Operations and Reports, 1215 Jefferson Davis Highway, Suite 1204, Arlington VA 22202-4302. Respondents should be aware that notwithstanding any other provision of law, no person shall be subject to a penalty for failing to comply with a collection of information if it does not display a currently valid OMB control number.

1. REPORT DATE	2. REPORT TYPE	3. DATES COVERED
APR 2014		**00-00-2014 to 00-00-2014**

4. TITLE AND SUBTITLE	5a. CONTRACT NUMBER
Development and Evaluation of a Hydrostatic Dynamical Core using the Spectral element/Discontinuous Galerkin Methods	5b. GRANT NUMBER
	5c. PROGRAM ELEMENT NUMBER
6. AUTHOR(S)	5d. PROJECT NUMBER
	5e. TASK NUMBER
	5f. WORK UNIT NUMBER
7. PERFORMING ORGANIZATION NAME(S) AND ADDRESS(ES) **Naval Postgraduate School,Department of Applied Mathematics,Monterey,CA,93943**	8. PERFORMING ORGANIZATION REPORT NUMBER
9. SPONSORING/MONITORING AGENCY NAME(S) AND ADDRESS(ES)	10. SPONSOR/MONITOR'S ACRONYM(S)
	11. SPONSOR/MONITOR'S REPORT NUMBER(S)

12. DISTRIBUTION/AVAILABILITY STATEMENT
Approved for public release; distribution unlimited

13. SUPPLEMENTARY NOTES

14. ABSTRACT

In this paper, we present a dynamical core for the atmospheric primitive hydrostatic equations using a unified formulation of spectral element (SE) and discontinuous Galerkin (DG) methods in the horizontal direction with a finite difference (FD) method in the radial direction. The CG and DG horizontal discretization employs high-order nodal basis functions associated with Lagrange polynomials based on Gauss-Lobatto-Legendre (GLL) quadrature points, which define the common machinery. The atmospheric primitive hydrostatic equations are solved on the cubed-sphere grid using the flux form governing equations three-dimensional (3D) Cartesian space. By using Cartesian space, we can avoid the pole singularity problem due to spherical coordinates and this also allows us to use any quadrilateral-based grid naturally. In order to consider an easy way for coupling the dynamics with existing physics packages, we use a FD in the radial direction. The models are verified by conducting conventional benchmark test cases: the Rossby-Haurwitz wavenumber 4 Jablonowski-Williamson tests for balanced initial state and baroclinic instability, and Held- Suarez tests. The results from those tests demonstrate that the present dynamical core can produce numerical solutions of good quality comparable to other models..

15. SUBJECT TERMS

16. SECURITY CLASSIFICATION OF:			17. LIMITATION OF ABSTRACT	18. NUMBER OF PAGES	19a. NAME OF RESPONSIBLE PERSON
a. REPORT	b. ABSTRACT	c. THIS PAGE			
unclassified	**unclassified**	**unclassified**	**Same as Report (SAR)**	**39**	

Abstract

In this paper, we present a dynamical core for the atmospheric primitive hydrostatic equations using a unified formulation of spectral element (SE) and discontinuous Galerkin (DG) methods in the horizontal direction with a finite difference (FD) method in the radial direction. The CG and DG horizontal discretization employs high-order nodal basis functions associated with Lagrange polynomials based on Gauss-Lobatto-Legendre (GLL) quadrature points, which define the common machinery. The atmospheric primitive hydrostatic equations are solved on the cubed-sphere grid using the flux form governing equations in a three-dimensional (3D) Cartesian space. By using Cartesian space, we can avoid the pole singularity problem due to spherical coordinates and this also allows us to use any quadrilateral-based grid naturally. In order to consider an easy way for coupling the dynamics with existing physics packages, we use a FD in the radial direction. The models are verified by conducting conventional benchmark test cases: the Rossby-Haurwitz wavenumber 4, Jablonowski-Williamson tests for balanced initial state and baroclinic instability, and Held-Suarez tests. The results from those tests demonstrate that the present dynamical core can produce numerical solutions of good quality comparable to other models..

1. Introduction

Spectral element (SE; here after is referred to as continuous Galerkin (CG)) and discontinuous Galerkin (DG) methods are very attractive on many-core computing platforms because these methods decompose the physical domain into smaller pieces having a small communication footprint. CG/DG methods are local in nature and thus can have a large on-processor operation count (Kelly and Giraldo, 2012) which is advantageous on large processor-count computers. Also CG/DG methods can achieve high-order accuracy because the polynomial order can be adjusted automatically according to the corresponding numerical integration rule, that is, the Gaussian quadrature (Taylor et al. 1997; Giraldo 2001; Giraldo et al. 2002). In addition, CG/DG methods are geometrically flexible in the types of grids they can use; this includes static and adaptive grids as well as conforming and non-conforming grids (Giraldo et al. 2002; Giraldo and Rosmond 2004; Mueller et al. 2013).

The CG method is characterized by the high-order approximation combined with the local decomposition property of the finite element method (FEM) and weak numerical dispersion property of the spectral method. The DG method, on the other hand, is best characterized as a combination of the properties of the CG method plus the local conservation properties of the finite volume method (FVM) (Giraldo and Restelli 2008). The virtues of the DG method are that it is inherently conservative (both locally and globally) as in the case of the FVM. However, the common criticism of the DG method is the stringent Courant-Friedrichs-Lewy (CFL) stability constraint in explicit time schemes. For a DG method using k-th order basis functions, an approximate CFL limit estimate is 1/(2k+1) (Cockburn and Shu 1989). This, however, is partly due to the choice of the numerical flux which, for expediency, is chosen as a purely edge-based flux although other fluxes are also possible (e.g., Yelash et al. 2014); however these more sophisticated approaches come at a price and it is yet unclear

66 which strategy yields a faster wallclock time to solution.

67 To date, successful applications of the CG method in hydrostatic atmospheric modeling
68 include the Community Atmosphere Model – spectral element dynamical core (CAM-SE)
69 (Dennis et al. 2012) and the scalable spectral element Eulerian atmospheric model (NSEAM)
70 (Giraldo and Rosmond, 2004, hereafter GR04). In this context, one of the motivations of this
71 study is to construct a dynamical core using a unified formulation of CG and DG methods as
72 described in Giraldo and Restelli 2008 and Kelly and Giraldo 2012 where nonhydrostatic
73 atmospheric models are proposed. Successful applications of the DG method in hydrostatic
74 atmospheric modeling include the work of Nair et al. 2009; however, in our paper we shall
75 present results for more than one test case. To our knowledge, the results for the Held-Suarez
76 test cases presented in our paper are the first such results shown for a DG model. The
77 significance is that this confirms the long-term stability of the DG method for hydrostatic
78 models. Although we could also discretize the vertical direction with CG and DG methods,
79 we choose a conservative flux-form finite-difference method for discretization in the vertical
80 direction which is similar to the approach used in both CAM-SE and NSEAM. This choice of
81 vertical discretization provides an easy way for coupling the dynamics with existing physics
82 packages.

83 In this paper we construct a unified formulation of CG and DG for the primitive
84 hydrostatic equations in GR04. In order to achieve a unified formulation, the advective-form
85 governing equations in GR04 are recast in flux form. GR04 provides a clue for converting the
86 advective-form equation set in 3D Cartesian space to the flux form in their appendix. By
87 using 3D Cartesian space, we can be free from the pole singularity problem in spherical
88 coordinates. Although a local Cartesian coordinate system could also be used to overcome
89 these problems (Taylor et al. 1997; Nair et al. 2005), the use of 3D Cartesian space
90 everywhere allows us to treat the pole as any other point. Therefore it permits general grids

91 naturally such as icosahedral, hexahedral, and adaptive unstructured grids (it should be noted
92 that general grids can also be used with the coordinate invariant form of the equations). In
93 this paper we adopt a hexahedral grid – the so called cubed-sphere.

94 In brief, the objective of this paper is to show the feasibility of the hydrostatic primitive
95 equation models using CG/DG horizontal discretization and the FD vertical discretization by
96 conducting conventional benchmark test cases. The organization of the remainder of this
97 paper is as follows. In the next section we describe the governing equations in 3D Cartesian
98 space with a definition of the prognostic and diagnostic variables. In Sec. 3 we explain the
99 horizontal, vertical, and temporal discretization methods including the numerical
100 approximation of the equations. In Sec. 4 we describe the cubed-sphere grid, and in Sec. 5,
101 we present the simulation results of the test cases. Finally, in Sec. 6, we end the paper with a
102 summary of our findings and some concluding remarks.
103

104 # 2. Governing Equations

105 The primitive hydrostatic equations of conservation form in the 3D Cartesian space with
106 a sigma pressure vertical coordinate σ are given as

107 $$\frac{\partial q}{\partial t} + \nabla \cdot \bar{\mathrm{F}} = \mathrm{S}_{Cor} + \mathrm{S}_h + \mathrm{S}_v \,, \tag{1}$$

108 where

109 $$q = \begin{bmatrix} \pi \\ U \\ V \\ W \\ \Theta \end{bmatrix} = \begin{bmatrix} \pi \\ \pi u \\ \pi v \\ \pi w \\ \pi\theta \end{bmatrix} \tag{2}$$

110 are prognostic variables,

111 $$\mathrm{S}_{Cor} = \begin{bmatrix} 0 \\ -\frac{2\omega z}{a^2}(yW - zV) - \mu x \\ -\frac{2\omega z}{a^2}(zU - xW) - \mu y \\ -\frac{2\omega z}{a^2}(xV - yU) - \mu z \\ 0 \end{bmatrix}, \ \mathrm{S}_h = \begin{bmatrix} 0 \\ (\phi - \Theta c_p \frac{\partial \mathrm{P}}{\partial \pi})\frac{\partial \pi}{\partial x} \\ (\phi - \Theta c_p \frac{\partial \mathrm{P}}{\partial \pi})\frac{\partial \pi}{\partial y} \\ (\phi - \Theta c_p \frac{\partial \mathrm{P}}{\partial \pi})\frac{\partial \pi}{\partial z} \\ 0 \end{bmatrix}, \ \mathrm{S}_v = \begin{bmatrix} -\frac{\partial}{\partial \sigma}(\pi \dot{\sigma}) \\ -\frac{\partial}{\partial \sigma}(U \dot{\sigma}) \\ -\frac{\partial}{\partial \sigma}(V \dot{\sigma}) \\ -\frac{\partial}{\partial \sigma}(W \dot{\sigma}) \\ -\frac{\partial}{\partial \sigma}(\Theta \dot{\sigma}) \end{bmatrix} \tag{3}$$

112 respectively denote Coriolis with the Lagrange multiplier μ, horizontal, and vertical source

113 terms, and

114 $$\bar{\mathrm{F}} = \begin{bmatrix} U \\ \frac{U^2}{\pi} + \pi\phi \\ \frac{VU}{\pi} \\ \frac{WU}{\pi} \\ \frac{\Theta U}{\pi} \end{bmatrix} \hat{i} + \begin{bmatrix} V \\ \frac{UV}{\pi} \\ \frac{V^2}{\pi} + \pi\phi \\ \frac{WV}{\pi} \\ \frac{\Theta V}{\pi} \end{bmatrix} \hat{j} + \begin{bmatrix} W \\ \frac{UW}{\pi} \\ \frac{VW}{\pi} \\ \frac{W^2}{\pi} + \pi\phi \\ \frac{\Theta W}{\pi} \end{bmatrix} \hat{k} \tag{4}$$

115 is the horizontal flux terms where $\hat{i}$, $\hat{j}$, and $\hat{k}$ denote the Cartesian directional unit

116 vectors. The prognostic variables q are comprised of: 1) the surface pressure π defined as

117 $$\pi = p_s - p_t, \tag{5}$$

118 where p_s is the true surface pressure, and p_t is the pressure at the top of the atmosphere; 2)

119 the flux-form velocity components $\mathbf{U} = (U, V, W) = (\pi u, \pi v, \pi w)$, where (u, v, w) are the

120 three Cartesian velocity components, and 3) the flux-form potential temperature $\Theta = \pi\theta$,

121 where θ is the potential temperature. The diagnostic variables are 1) the geopotential ϕ

122 given by the diagnostic equation as

$$\frac{\partial \phi}{\partial \mathrm{P}} = -c_p \theta, \tag{6}$$

2) the Exner function P defined as

$$\mathrm{P} = \left(\frac{p}{p_0} \right)^{R_d / c_p}, \tag{7}$$

where p and p_0 is the hydrostatic pressure and standard surface pressure, respectively, and R_d and c_p is the gas constant and specific heat of dry air at constant pressure, and 3) the σ-coordinate vertical velocity $\dot{\sigma} = \frac{d\sigma}{dt}$ where $\sigma = \frac{p - p_t}{\pi} \in [0,1]$ is the definition of the sigma pressure coordinate with a value of 0 at the top of the atmosphere and 1 at the surface. The constants a and ω in Eq. (4) are the Earth's radius and angular velocity, respectively, and μ is a Lagrange multiplier for the fluid particles to remain on a spherical shell with constant σ. The momentum variables representing the atmospheric motion over the shell in the Cartesian space have three components along the x, y, and z axes in Cartesian coordinates, so that the movement of a particle on the shell has three degrees of freedom, which can move freely in R^3. To ensure that fluid particles remain on the spherical shell, it is required that the fluid velocity remains perpendicular to the position vector, which yields a Lagrange multiplier in the momentum equations (Giraldo 2001; Giraldo et al. 2002; Giraldo and Rosmond, 2004). It is noteworthy that among the independent variables (x, y, z, σ, t), (x, y, z) represent grid points on the sphere which are related to the points in the spherical coordinates (λ, φ) given as

$$\begin{aligned} x &= a \cos\lambda \cos\varphi, \\ y &= a \sin\lambda \cos\varphi, \\ z &= a \sin\varphi. \end{aligned} \tag{8}$$

Thus ∇ is defined as

143 $$\nabla = \begin{pmatrix} \frac{\partial}{\partial x} \\ \frac{\partial}{\partial y} \\ \frac{\partial}{\partial z} \end{pmatrix} \quad (9)$$

144 at constant σ.

145

146 # 3. Discretization

147 1) Discretization in the horizontal direction

148 To describe the discretization of the horizontal operators by the CG/DG method we
149 follow the description given previously in Giraldo and Restelli 2008 and in Kelly and Giraldo
150 2012. Let us begin by rewriting Eq. (1) as follows

151 $$\frac{\partial q}{\partial t} + \nabla \cdot F = S \quad (10)$$

152 Next, let us introduce the following vector spaces

153 $$V^{CG} = \left\{ \psi \in H^1(\Omega) \middle| \psi \in P_N(\Omega_e) \right\} \quad (11)$$

154 and

155 $$V^{DG} = \left\{ \psi \in L^2(\Omega) \middle| \psi \in P_N(\Omega_e) \right\} \quad (12)$$

156 where we now seek solutions of Eq. (1) as follows:

157 $$q \in V \qquad \forall \psi \in V$$

158 where V denotes either V^{CG} or V^{DG}. Next, we approximate the solution vector as follows

159 $$q_N(x, y, z, t) = \sum_{i=1}^{M} \psi_i(x, y, z) q_i(t) \quad (13)$$

160 where, for quadrilateral elements in the horizontal direction, $M = (N+1)^2$ with N

representing the polynomial order of the basis function ψ.

We now introduce this expansion into our governing system of equations, multiply by a test function, and integrate by parts to yield

$$\int_{\Omega_e} \psi_i \frac{\partial q_N}{\partial t} d\Omega_e + \int_{\Gamma_e} \psi_i \hat{n} \cdot F d\Gamma_e - \int_{\Omega_e} \nabla \psi_i F(q_N) d\Omega_e = \int_{\Omega_e} \psi_i S(q_N) d\Omega_e . \qquad (14)$$

where the terms with Ω_e refer to volume integrals and the one with Γ_e is a boundary integral which accounts for both internal faces (neighboring elements share faces) as well as boundary faces (elements on boundaries do not share faces with other elements). In matrix-vector form, this equation can be written as

$$M^e_{i,j} \frac{dq^e_j}{dt} + \left(\mathbf{M}^{f,e}_{i,j}\right)^T F^*_j(q_N) - \left(\mathbf{D}^{\xi}_{i,j}\right)^T F_j(q^e_N) = S_i(q^e_N) \qquad (15)$$

where

$$\begin{aligned} M^e_{i,j} &= \int_{\Omega_e} \psi_i \psi_j d\Omega_e , \\ \mathbf{M}^{f,e}_{i,j} &= \int_{\Gamma_e} \psi_i \psi_j \hat{n} d\Gamma_e , \\ \mathbf{D}^{\xi}_{i,j} &= \int_{\Omega_e} \nabla \psi_i \psi_j d\Omega_e . \end{aligned} \qquad (16)$$

These matrices represent: the mass, flux, and differentiation matrices, respectively.

For the DG method, the matrix-vector form given above is sufficient as long as we define the numerical flux , e.g., as follows

$$F^*(q_N) = \frac{1}{2}\left[F(q^L_N) + F(q^R_N) - \hat{n}\left|\lambda_{\max}\right|\left(q^R_N - q^L_N\right)\right] \qquad (17)$$

where the superscripts L and R refer to the left and right elements (arbitrarily decided) of the face Γ_e and $\lambda_{\max}$ is the maximum eigenvalue of the Jacobian matrix of the governing partial differential equations. Here we use the Rusanov scheme for the numerical flux because of its simplicity although any other Riemann solver could be used. For the CG method, the matrix-vector form given above is also used except that the term of the flux

matrix vanishes on the sphere and we then use the direct stiffness summation (DSS) operation which gathers the element-wise solution to a global grid point solution and then scatters it back to the element-wise space. This is done to ensure that the solution is C^0 across all element faces.

2) Discretization in the vertical direction

We use the FD method similarly to other global models to gain an easy way for coupling the dynamics with existing physics packages, although we could also discretize the vertical operators with the CG/DG methods (as done in Kelly and Giraldo 2012; Giraldo et al. 2013). Also by using the FD, we can keep the model as similar as possible to the NSEAM model (GR04) so that we directly discern differences from the discrete horizontal operators. Using a Lorenz staggering, the variables U, V, W, Θ, and ϕ are at layer mid points denoted by $k = 1, 2, \ldots, Nlev$ where $Nlev$ is the total number of layers, while the variable P and $\dot{\sigma}$ are at layer interface points denoted by $k + \frac{1}{2}$, $k = 0, 1, \ldots, Nlev$.

We begin the vertical discretization by the evaluating $\frac{\partial \pi}{\partial t}$ which is given by integrating the first row of Eq. (1) (i.e., the continuity equation) from the surface ($\sigma_{bottom} = \sigma_{Nlev+1/2} = 1$) to the top ($\sigma_{top} = \sigma_{1/2} = 0$) with no-flux boundaries at the top and bottom levels of the atmosphere (i.e. $\dot{\sigma}_{top} = \dot{\sigma}_{bottom} = 0$). Thus,

$$\frac{\partial \pi}{\partial t} = \mathbf{M}^{-1} \sum_{k=1}^{Nlev} \mathbf{D}^{\Omega} \mathbf{U}_k \Delta\sigma_k \,, \tag{18}$$

where k is the number of vertical levels to be integrated across and $\Delta\sigma_l = \sigma_{l+1/2} - \sigma_{l-1/2}$ is the thickness of the layer. Then the vertical velocity $\dot{\sigma}$ at each vertical level is obtained by integrating the continuity equation from the top of the atmosphere to the material surface as

follows

$$(\dot{\sigma}\pi)_{k+1/2} = -\frac{\partial \pi}{\partial t}\sigma_{k+1/2} + \mathrm{M}^{-1}\sum_{l=1}^{k}\dot{\mathrm{D}}\cdot \mathrm{U}_l \Delta\sigma_l \,. \tag{19}$$

The vertical advection term $\frac{\partial(\dot{\sigma}q)}{\partial\sigma}$ in the vertical source term S_v is computed using the third-order upwind biased discretization in Hundsdorfer et al. (1995) which is given as

$$\left.\frac{\partial f}{\partial \sigma}\right|_k = \frac{f_{k-2} - 8f_{k-1} + 8f_{k+1} - f_{k+2}}{12\Delta\sigma} + \mathrm{sign}(\dot{\sigma}_k)\frac{f_{k-2} - 4f_{k-1} + 6f_k - 4f_{k+1} + f_{k+2}}{12\Delta\sigma}, \tag{20}$$

where f denotes the flux $(\dot{\sigma}q)$. It is noted that the upwind-biased schemes are inherently diffusive. Following GR04, the hydrostatic equation, Eq. (6), is evaluated as follows

$$\phi_k - \phi_{k+1} = c_p \Theta_k (\mathrm{P}_{k+1/2} - \mathrm{P}_k) + c_p \Theta_{k+1}(\mathrm{P}_{k+1} - \mathrm{P}_{k+1/2}), \tag{21}$$

where the Exner function at layer interfaces and midpoints is given by

$$\mathrm{P}_{k+1/2} = \left(\frac{p_{k+1/2}}{p_0}\right)^{\kappa} \tag{22}$$

and

$$\mathrm{P}_k = \frac{1}{\kappa+1}\frac{1}{p_0^{\kappa}}\left(\frac{p_{k+1/2}^{\kappa+1} - p_{k-1/2}^{\kappa+1}}{p_{k+1/2} - p_{k-1/2}}\right), \tag{23}$$

respectively.

3) Discretization in time

For integrating the equations, we adopt a third-order strong stability preserving explicit Runge-Kutta (SSP-RK) scheme (Cockburn and Shu 1998; Nair et al. 2005). The 3rd order SSP-RK scheme is introduced into our governing equations in the form of

$$\frac{\partial q}{\partial t} = R(q), \tag{24}$$

and is given as follows:

$$
\begin{aligned}
q^{(1)} &= q^{n} + \Delta t\, \mathrm{R}(q^{n}) \\
q^{(2)} &= \frac{3}{4} q^{n} + \frac{1}{4} q^{(1)} + \frac{1}{4} \Delta t\, \mathrm{R}(q^{(1)}) \\
q^{n+1} &= \frac{1}{3} q^{n} + \frac{2}{3} q^{(1)} + \frac{2}{3} \Delta t\, \mathrm{R}(q^{(2)}),
\end{aligned}
\tag{25}
$$

where the superscripts n and $n+1$ denote time levels t and $t+\Delta t$, respectively. While for smooth problems the SSP-RK scheme does not generate spurious oscillations so that are widely used for DG methods, for problems with strong shocks or discontinuities, oscillations can lead to nonlinear instabilities (Cockburn and Shu 1998). Since an SSP-RK time-integration scheme cannot control such undesirable effects, a Boyd-Vandeven spatial filter is applied after the time integration, which is described in GR04. Neither viscosity nor slope limiter are used in all simulations.

4. Cubed-sphere Grid

The cubed-sphere grids are composed of the six patches obtained by the gnomonic projection of the faces of the hexahedron which are subdivided into $(n_H \times n_H)$ quadrilateral elements where n_H is the number of quadrilateral elements in each direction (GR04). Inside each element we build $(N+1)$ Gauss-Lobatto-Legendre (GLL) quadrature points, where N indicate the polynomial order of the basis function ψ. Therefore the total number of grid points N_p is given as

$$
N_p = 6\left(n_H N\right)^2 + 2, \tag{26}
$$

and the number of elements N_e comprising the sphere is

$$
N_e = 6\left(n_H\right)^2. \tag{27}
$$

We now introduce the square region on the gnomonic space $\left(\xi_G, \eta_G\right) = \left[-\frac{\pi}{4}, +\frac{\pi}{4}\right]^2$ in each of the six faces to describe the relation to spherical coordinates $\left(\lambda, \varphi\right)$. The gnomonic space $\left(\xi_G, \eta_G\right) = \left[-\frac{\pi}{4}, +\frac{\pi}{4}\right]^2$ is mapped to the corresponding spherical coordinates $\left(\lambda_G, \varphi_G\right)$ via

$$\lambda_G = \xi_G, \tag{28}$$

$$\varphi_G = \arcsin\left(\frac{\tan\eta_G}{\sqrt{1+\tan^2\xi_G + \tan^2\eta_G}}\right), \tag{29}$$

and then we construct the cubed-sphere grid by rotating this face to the six faces of the hexahedron by

$$\lambda = \lambda_c + \arctan\left(\frac{\cos\varphi_G \sin\lambda_G}{\cos\varphi_G \cos\lambda_G \cos\varphi_c - \sin\varphi_G \sin\varphi_c}\right), \tag{30}$$

$$\varphi = \arcsin\left(\sin\varphi_G \cos\varphi_c + \cos\varphi_G \cos\lambda_G \sin\varphi_c\right), \tag{31}$$

with the centroids, $\left(\lambda_c, \varphi_c\right) = \left(\left[c-1\right]\frac{\pi}{2}, 0\right)$ for $c = 1, \mathrm{K}, 4$, $\left(\lambda_5, \varphi_5\right) = \left(0, \frac{\pi}{2}\right)$, and $\left(\lambda_6, \varphi_6\right) = \left(0, -\frac{\pi}{2}\right)$.

The resolution of the cubed-sphere grid H is determined by n_H (the number of quadrilateral elements in each direction contained in each of the six faces of the cube) and N (the polynomial order of the elements), where we use $H = n_H N$ as the convention to define the grid resolution. Fig. 1 show examples of the grids with $H = 3$ ($n_H = 3$ and $N = 1$), $H = 15$ ($n_H = 3$ and $N = 5$), and $H = 35$ ($n_H = 5$ and $N = 7$).

5. Simulation results with Benchmark Tests

We consider the following test cases: 1) 3D Rossby-Haurwitz wavenumber 4, 2) Jablonowski-Williamson balanced initial state test, 3) baroclinic instability test, and 4) Held-Suarez test. Because all of the test cases except 2) the Jablonowski-Williamson balanced initial state test do not have analytical solutions, we compare our results to the results of other published papers and evaluate the results qualitatively. We now discuss the results of the four test cases.

1) 3D Rossby-Haurwitz wavenumber 4

We conduct the Rossby-Haurwitz (RH) wave test case which is a 3D extension of the 2D shallow water RH wave discussed in Williamson et al. (1992). The main differences compared to the 2D shallow water formulation include the introduction of a temperature field and the derivation of the surface pressure, which is discussed in GR04 and Jablonowski et al. (2008). The Rossby-Haurwitz wave approximately preserves its shape even in nonlinear shallow water and primitive equation models, which has a sufficiently simple enough pattern to allow one to judge if the simulation was successful. We initialize the model following Jablonowski et al. (2008).

Snapshots of the output data for the CG and DG models for day 15 are presented in Figs. 2 and 3, respectively. The figures show the 850 hPa zonal wind, meridional wind, and temperature as well as the surface pressure. These model results were computed at the resolution of $H = 64$ ($n_H = 8$ and $N = 8$) with 26 vertical levels (Nlev=26). The results of the CG and DG simulations are virtually indistinguishable; in addition, the accuracy results of both simulations are almost identical to the results obtained with the CAM3.5.41 version

283 of the NCAR Finite Volume (FV) dynamical core at the resolution 1° by 1° with 26 hybrid
284 levels, as described in Jablonowski et al. (2008). Although we have used a relatively low
285 resolution of H64 which is comparable to T63 of a spectral model, the results are strikingly
286 similar to the solutions with the 1°x1° NCAR CAM-FV core, both in phase and amplitude.
287
288 2) Jablonowski-Williamson balanced initial state test
289 In order to estimate the accuracy and stability of the dynamical core, we conduct the
290 Jablonowski-Williamson balanced initial state test introduced by Jablonowski and
291 Williamson (2006). We initialize the model following Jablonowski and Williamson (2006a
292 and b). Using the balanced initial fields, the simulation results should maintain the initial state
293 perfectly for a sufficient amount of time. Since the initial state of this test is the true solution,
294 we can compute error norms. We evaluate the error by using the relative L_2 error defined by

295 $$\left\| q_{simulation} \right\|_{L_2} = \sqrt{\frac{\int_\Omega \left(q_{exact} - q_{simulation} \right)^2 d\,\Omega}{\int_\Omega q_{exact}^2 d\,\Omega}},$$

296 where $q_{simulation}$ represents the computed state variables and q_{exact} the exact (i.e., initial
297 condition) values.
298 Figure 4 shows the normalized surface pressure L_2 error norms for the CG and DG
299 simulations with $H = 128$ ($n_H = 16$ and $N = 8$) horizontal resolution and 26 vertical
300 levels (Nlev=26). The L_2 error norms of the two simulations are visually identical, in which
301 the error oscillates but remains bounded. These results (including the value of the L_2 error)
302 compare well against those of the NSEAM model presented in GR04. The bounded error
303 confirms that the initial balanced state is properly maintained. In practice though, the initial
304 state degrades over time. After 20-days, the zonal wind fields for the CG and DG simulations
305 show a somewhat distorted distribution with an increasing zonally asymmetric pattern (Fig.

306 5). Initially the maximum of the zonal winds at the lowest level are about 9.4 m/s in mid-
307 latitude, but after 20-days the maximum difference of the zonal wind is up to about 0.02 m/s
308 showing the zonal asymmetry. Although the error distribution is different between the CG
309 and DG simulations in detail, these have a wavenumber 4 structure which arise from the
310 cubed-sphere grid. The wavenumber 4 signals grow over time and lead eventually to a
311 breakdown of the balanced state. However, higher resolutions delay the growth of the signals
312 as the truncation error associated with the spatial discretization decreases. Actually, at
313 $H = 192$ ($n_H = 16$ and $N = 12$) horizontal resolution this error virtually disappears for
314 20-day simulations (Fig. 6).
315
316 3) Jablonowski-Williamson baroclinic instability test
317 The baroclinic instability test case starts from the balanced initial fields, which is
318 described above, with a perturbation in the initial zonal velocity. The baroclinic wave is
319 induced by the small perturbation in the initial zonal wind. Here a Gaussian profile is used for
320 the zonal wind perturbation, which is centered at $(\lambda_c, \varphi_c) = \left(\frac{\pi}{9}, \frac{2\pi}{9}\right)$ pointing to the
321 location $\left(20^{\circ}\mathrm{E}, 40^{\circ}\mathrm{N}\right)$. This perturbation is given by

322 $$u_{perturbation}(\lambda, \varphi, \sigma) = \exp\left[-\left(\frac{r}{R}\right)^2\right],$$

323 where

324 $$r = a \arccos\left[\sin\varphi_c \sin\varphi + \cos\varphi_c \cos\varphi \cos\left(\lambda - \lambda_c\right)\right],$$

325 and $R = a/10$ is the perturbation radius (Jablonowski and Williamson 2006a and b).
326 Since the baroclinic wave test case does not have an analytic solution, we compare our
327 results to the solutions from Jablonowski and Williamson (2006a) and the NSEAM model in

328 GR04. We show the surface pressure, 850 hPa temperature, and 850 hPa relative vorticity at
329 day 9 for the CG and DG simulations with the resolution of $H = 80$ ($n_H = 16$ and
330 $N = 5$) and 26 vertical levels (Nlev=26) in Fig. 7 which can be compared with the solutions
331 of the National Center for Atmospheric Research's Community Atmosphere Model version 3
332 (NCAR CAM3) Eulerian dynamical core at T85 resolution and finite volume core at 1° by
333 1.25° from Jablonowski and Williamson (2006a). The CG and DG simulations in Fig. 7 are
334 visually very similar to those reported in Jablonowski and Williamson with regard to the
335 structure in the fields and the extrema for the surface pressure; in addition, the CG and DG
336 results are almost identical to each other. Differences, however, can only be seen in the
337 relative vorticity field at very small scales. In the CG simulation, the small-scale vorticity in
338 the vicinity of the hook is depicted, and the maximum strength of the relative vorticity is
339 larger than that of the DG simulation, which can be also seen in the results of a relatively
340 higher resolution shown in Fig. 8. Figure 8 shows the same fields at day 9 as in Fig. 7 but for
341 the higher resolution of $H = 160$ ($n_H = 32$ and $N = 5$) and 26 vertical levels (Nlev=26).
342 In comparison with the results of the lower resolution of $H = 80$ ($n_H = 16$ and $N = 5$), it
343 can be clearly seen that the numerical solutions of the two different resolutions are well
344 converged in terms of the strength and structure in the surface pressure, temperature, and
345 vorticity fields. It is noted that the vorticity fields in the higher resolution are characterized by
346 the smallest scale in the vicinity of the hook, which is the same as in the lower resolution,
347 which imply that the DG simulation is more diffusive than the CG simulation. It suggests that
348 the diffusive property of the DG simulation is induced by the Rusanov numerical flux used in
349 this study, because the only difference between the CG and DG formulations is the numerical
350 flux and the fact that the DG solutions are allowed to contain jumps across element edges.
351 However, this difference in the results suggests that it is the dissipation of the numerical flux

352 that is mainly responsible for the differences in the two simulations.

353 In general, the baroclinic wave grows observably around day 4. At day 7 the baroclinic
354 wave evolves rapidly and by day 9 the wave train has intensified significantly (Jablonowski
355 and Williamson 2006a). In order to examine the growth of the perturbation, an evolution of
356 the minimum surface pressure is shown in Fig. 9 which we now compare with the results in G
357 R04. The results of the CG and DG simulations with different resolutions are almost in
358 agreement until day 10, at which point the simulations begin to show slight deviations from
359 each other. The DG simulation with the lower resolution tends to simulate somewhat weak
360 deepening. During the period between day 10 and 11 when wave breaking has set in, the
361 remarkable weak deepening is shown in the DG simulation at the lower resolution. At day 14,
362 the difference of the minimum surface pressure between the DG simulation at the lower
363 resolution and the three other simulations is about 2 hPa.

364

365 4) Held-Suarez test

366 In order to estimate the capabilities of the model in simulating a realistic climate
367 circulation without complex parameterizations, we conduct the Held-Suarez test. The Held-
368 Suarez test ensures that a dynamical core produces a realistic zonal and time mean climate
369 and synoptic eddies by using a simple Newtonian relaxation of the temperature field and a
370 Rayleigh damping of low-level winds representing boundary-layer friction (Held and Suarez
371 1994). The Newtonian relaxation of the temperature is added as the diabatic forcing term to
372 the thermodynamic equation, the fifth row of Eq. (1), and the Rayleigh damping is imposed
373 as dissipation term in the momentum equation, the second to fourth rows of Eq. (1). The
374 detailed specifications are adapted from Held and Suarez (1994). For this test we use a
375 relatively low resolution of $H = 40$ ($n_H = 8$ and $N = 5$) with 25 vertical levels
376 (Nlev=25) because this test case requires a relatively long model time simulation for 1200

377 days. In this paper, the integrations start from a stably stratified state at rest atmosphere, in
378 which the lapse rate of temperature is 6.5 K/m and the surface temperature is 288 K. We use
379 the simulation results from day 200 to day 1200 integrations sampled every 10-days.

380 Fig. 10 shows the time mean zonally averaged zonal wind and temperature for both the
381 CG and DG simulations which can be easily compared to the results of other published
382 papers. In comparison with the results of the spectral transform model in Held and Suarez
383 (1994), both the CG and DG simulations show reasonable and comparable distributions,
384 where the midlatitude jets at the upper troposphere near 250 hPa and the equatorial easterly
385 flow in the lower and upper atmosphere are clearly visible in each hemisphere. Also
386 temperature stratification is maintained realistically. The simulation results are comparable to
387 that of GR04. There exist, however, differences between the results of the CG and DG
388 simulations mainly in the strength of the westerly flow and the temperature structure in the
389 upper atmosphere. DG simulates broader upper-level jet streams than CG that strengthen with
390 altitude. Also in the temperature field, the DG simulation shows warmer air in the equatorial
391 upper atmosphere. The difference is shown clearly in Fig. 11 where we plot the time mean
392 zonally averaged eddy heat flux of the CG and DG simulations. There are two maxima at
393 mid-latitude in the lower and upper atmosphere indicating transportations of heat in the
394 poleward direction, of which the distributions in the CG and DG simulations are in good
395 agreement with previous studies, for example, Held and Suarez (1994), Lin (2004) and Wan
396 et al. (2008). However, in comparison of the strength and horizontal gradient of the eddy heat
397 flux between both simulations, CG simulates a stronger eddy motion than DG.
398

399 # 6. Summary and Conclusions

400 We have proposed a hydrostatic dynamical solver using both the continuous Galerkin

(CG) and discontinuous Galerkin (DG) methods. It is solved on a cubed-sphere grid in 3D Cartesian coordinates although in principle any quadrilateral-based grid could be used. The CG and DG horizontal discretization employs a high-order nodal (Lagrange) basis function based on quadrilateral elements and GLL quadrature points which compose the common machinery. However, the DG method use fluxes along the boundaries of the elements which are approximated by the Rusanov method. In the vertical direction, a conservative flux-form finite-difference method is employed for coupling the dynamics with existing physics packages easily; we hope to report progresses on this specific topic in the future. A third-order strong stability preserving Runge-Kutta scheme was used for time integration although other time-integrators (including semi-implicit methods) could also be used.

In this paper, we show simulations of the model using four baroclinic test cases including: the Rossby-Haurwitz wave, balanced initial state, baroclinic instability, and Held-Suarez test cases. All cases, except for the Jablonowski-Williamson balanced initial state test case, do not have analytic solutions. Therefore, we compare our results to the results of test cases run by a vast community. Through our comparison of the CG and DG simulations, we show that for the baroclinic instability test and Held-Suarez test cases, the DG simulation tends to simulate somewhat weaker small-scale features, such as the minimum surface pressure perturbation and eddy heat flux, than the CG method. This could be due to the intrinsic diffusion of the Rusanov numerical flux scheme used for the horizontal discretization of the DG method, which is the only difference between the CG and DG formulations. One of the valuable contributions of this model is that we can use it to study the effects of using different horizontal discretizations since we use the exact same model with the same finite difference method in the vertical and time-integration methods but use either CG or DG in the horizontal. The discrete operators in the horizontal use the exact same numerical machinery and so the results shown here isolate the differences offered by the CG

and DG methods. However, for the other two test cases (Rossby-Haurwitz wave and balanced initial state tests), the results of the CG and DG simulations are virtually indistinguishable. Furthermore, the numerical results obtained for all four test cases show that the present dynamical core can produce numerical solutions of good quality comparable to other models. The results confirm that the CG and DG methods combined with the finite difference method in the vertical direction offer a viable strategy for atmospheric modeling. To our knowledge, we present the first results for a DG model for long-time simulations represented by the Held-Suarez test case. The importance of this result is that this confirms the stability of the DG method for long-time simulations in hydrostatic atmospheric dynamics. In order to make the model efficient and competitive with operational models, we need a semi-implicit time integration method which, although requires some additional machinery to be added, does not pose any theoretical barriers since such algorithms have already been designed by one of the authors in previous papers (Giraldo 2005, Giraldo et al. 2013).

Acknowledgements

This work was funded by Korea's Numerical Weather Prediction Model Development Project approved by Ministry of Science, ICT and Future Planning (MSIP). The first author is grateful for the MA4245 course (taught by F.X. Giraldo) which laid out the framework for the unified CG/DG approach. The second author gratefully acknowledges the support of KIAPS, the Office of Naval Research through program element PE-0602435N and the National Science Foundation (Division of Mathematical Sciences) through program element 121670.

References

Cockburn, B. and C. Shu, 1998: The Runge-Kutta discontinuous Galerkin finite element method for conservation laws. V: Multidimensional systems. J. Comput. Phys., 141, 199–224.

Dennis, J. M., J. Edwards, K. J. Evans, O. Guba, P. H. Lauritzen, A. A. Mirin, A. St-Cyr, M. A. Taylor, and P. H. Worley, 2012: CAM-SE: A scalable spectral element dynamical core for the Community Atmosphere Model. Int. J. High Perf Comput Appl 26: 74-89.

Giraldo, F. X., 2001: A spectral element shallow water model on spherical geodesic grids. Int. J. Numer. Meth. Fluids, 35, 869–901.

Giraldo, F. X., J. S. Hesthaven, and T. Warburton, 2002: Nodal High-Order Discontinuous Galerkin Methods for the Spherical Shallow Water Equations. Journal of Computational Physics, 181, 499–525.

Giraldo, F. X., and T. E. Rosmond, 2004: A Scalable Spectral Element Eulerian Atmospheric Model (SEE-AM) for NWP: Dynamical Core Tests. Mon. Wea. Rev., 132, 133-153.

Giraldo, F. X., 2005: Semi-implicit Time-Integrators for a Scalable Spectral Element Atmospheric Model, Quart. J. Roy. Meteor. Soc., Vol. 131, 2431-2454.

Giraldo, F. X., and M. Restelli, 2008: A study of spectral element and discontinuous Galerkin methods for the Navier-Stokes equations in nonhydrostatic mesoscale atmospheric modeling: equation sets and test cases. Journal of computational physics 227, 3849-3877.

Giraldo, F. X., J. F. Kelly, and E. M. Constantinescu, 2013: Implicit-Explicit Formulations for a 3D Nonhydrostatic Unified Model of the Atmosphere (NUMA). SIAM J. Sci. Comp. 35 (5), B1162-B1194.

Held, I. M., and M. J. Suarez, 1994: A proposal for the intercomparison of the dynamical cores of atmospheric general circulation models. Bull. Amer. Meteor. Soc., 75, 1825-1830.

Hundsdorfer, W., B. Koren, M. van Loon, and K. G. Verwer, 1995: A positive finite-difference advection scheme. Journal of Computational Physics, 117, 35-46.

Jablonowski, C. and D. L. Williamson, 2006: A baroclinic instability test case for atmospheric model dynamical cores. Quart. J. Roy. Meteor. Soc., 132, 2943-2975.

Jablonowski, C., P. Lauritzen, R. Nair, and M. Taylor, 2008: Idealized test cases for the dynamical cores of atmospheric general circulation models: A proposal for the ncar asp 2008 summer colloquiumi. Manuscript May/29/2008, to be submitted as an NCAR Technical Report and journal paper.

Kelly, J. F. and F. X. Giraldo, 2012: Continuous and discontinuous Galerkin methods for a scalable three-dimensional nonhydrostatic atmospheric model: Limited-area mode. Journal of Computational Physics, 231, 7988–8008.

Lin, S.-J., 2004: A "vertically Lagrangian" finite-volume dynamical core for global models. Mon. Wea. Rev., 132, 2293-2307.

Müller, A., J. Behrens, F. X. Giraldo, and V. Wirth, 2013: Comparison between adaptive and uniform discontinuous Galerkin simulations in dry 2D bubble experiments. J. Comput. Phys., 235, 371-393.

Nair, R. D., S. J. Thomas, and R. D. Loft, 2005: A discontinuous Galerkin global shallow water model. Mon. Wea. Rev., 133, 876-888

Nair, R. D., H.-W. Choi, and H.M. Tufo, 2009: Computational aspects of a scalable high-order discontinuous Galerkin atmospheric dynamical core. Computers and Fluids, 38, 309–319.

Taylor, M., J. Tribbia, and M. Iskandarani, 1997: The spectral element method for the shallow water equations on the sphere. Journal of computational physics 130, 92-108.

Wan, H., M. A. Giorgetta, L. Bonaventura, 2008: Ensemble Held-Suarez test with a spectral transform model: variability, sensitivity, and convergence. Mon. Wea. Rev.,

136, 1075-1092.

Williamson, D. L., J. B. Drake, J. Hack, R. Jacob, and P. N. Swartztrauber, 1992: A standard test set for numerical approximations to the shallow water equations in spherical geometry. J. Comput. Phys., 102, 211-224.

Yelash, L., A. Muller, M. Lukacova-Medvidova, F.X. Giraldo, and V. Wirth, 2014: Adaptive discontinuous evolution Galerkin method for dry atmospheric flow. Journal of computational physics 268, 106–133.

Figure Captions

FIG. 1. The cubed-sphere grid for (a) the $H = 3$ ($n_H = 3$ and $N = 1$), (b) the $H = 15$ ($n_H = 3$ and $N = 5$), and (c) the $H = 35$ ($n_H = 5$ and $N = 7$) horizontal resolutions.

FIG. 2. Numerical results for the CG simulation on the resolution of the $H = 64$ ($n_H = 8$ and $N = 8$) with 26 vertical levels: Top row: 850 hPa zonal wind and meridional wind, bottom row: surface pressure and 850 hPa temperature.

FIG. 3. As in Fig. 2 but for the DG simulation.

FIG. 4. L2 error norm of surface pressure in Pa for the CG and DG simulations at the $H = 128$ ($n_H = 16$ and $N = 8$) horizontal resolution and 26 vertical levels.

FIG. 5. Distribution of zonal wind difference at the lowest model level between day 20 and day 0 for the (top) CG and (bottom) DG simulations at the $H = 128$ ($n_H = 16$ and $N = 8$) horizontal resolution and 26 vertical levels.

FIG. 6. As in Fig. 5 but for the $H = 192$ ($n_H = 16$ and $N = 12$) horizontal resolution.

FIG. 7. Baroclinic wave at day 9 with the (left) CG and (right) DG simulations with the resolution of the $H = 80$ ($n_H = 16$ and $N = 5$) horizontal resolution and 26 vertical

557 levels: (upper row) surface pressure, (middle row) 850 hPa temperature, and (bottom row)
558 850 hPa relative vorticity at days (left) 7 and (right) 9.
559
560 FIG. 8. As in Fig. 7 but for the $H = 160$ ($n_H = 32$ and $N = 5$).
561
562 FIG. 9. The minimum surface pressure (hPa) as a function of days for the CG and DG
563 simulations with the lower resolution of the $H = 80$ ($n_H = 16$ and $N = 5$) and the higher
564 resolution of the $H = 160$ ($n_H = 32$ and $N = 5$).
565
566 FIG. 10. The (left) mean zonally averaged zonal velocity (m/s) and (right) mean zonally
567 averaged temperature (K) for the (upper row) CG and (bottom row) DG simulations with the
568 resolution of the $H = 40$ ($n_H = 8$ and $N = 5$) and 25 vertical levels (Nlev=25). These
569 are calculated over the last 1000 days of a 1200-day integration.
570
571 FIG. 11. The mean zonally averaged eddy heat flux for the (left) CG and (right) DG
572 simulation with the resolution of the $H = 40$ ($n_H = 8$ and $N = 5$).
573

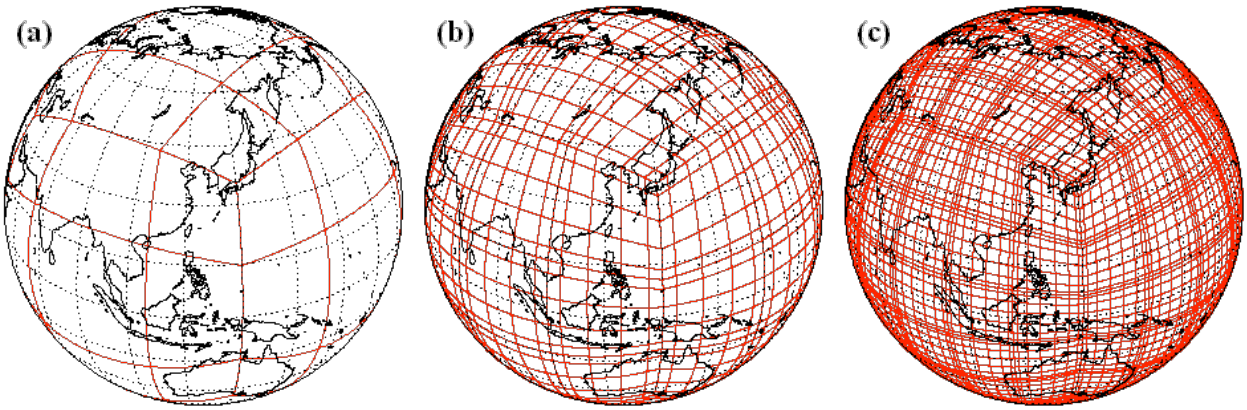

574

575 FIG. 1. The cubed-sphere grid for (a) the $H = 3$ ($n_H = 3$ and $N = 1$), (b) the

576 $H = 15$ ($n_H = 3$ and $N = 5$), and (c) the $H = 35$ ($n_H = 5$ and $N = 7$) horizontal

577 resolutions.

578

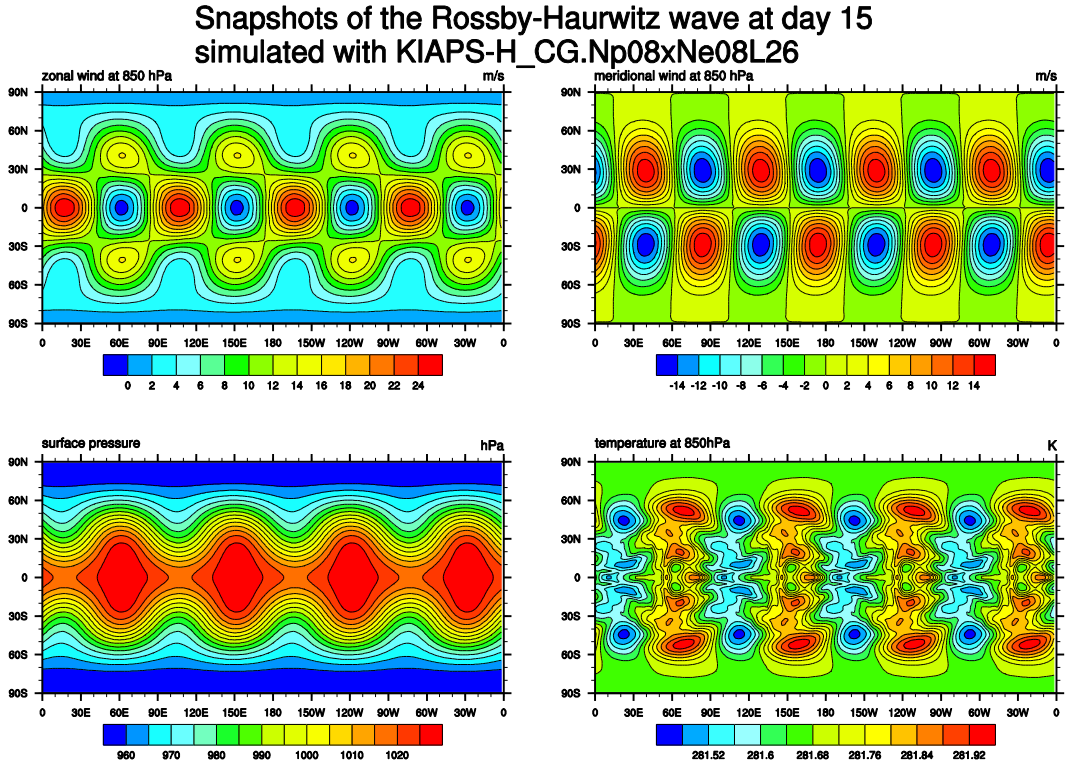

579

580 FIG. 2. Numerical results for the CG simulation on the resolution of the $H = 64$

581 ($n_H = 8$ and $N = 8$) with 26 vertical levels: Top row: 850 hPa zonal wind and meridional

582 wind, bottom row: surface pressure and 850 hPa temperature.

583

584

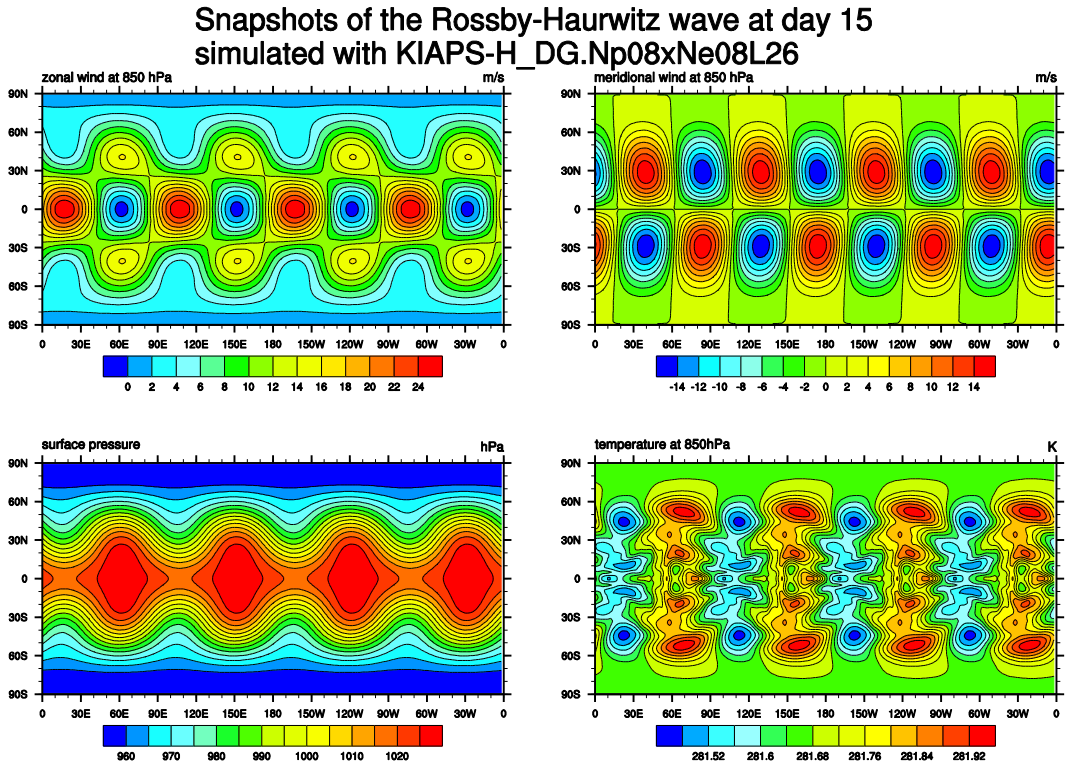

585

586 FIG. 3. As in Fig. 2 but for the DG simulation.

587

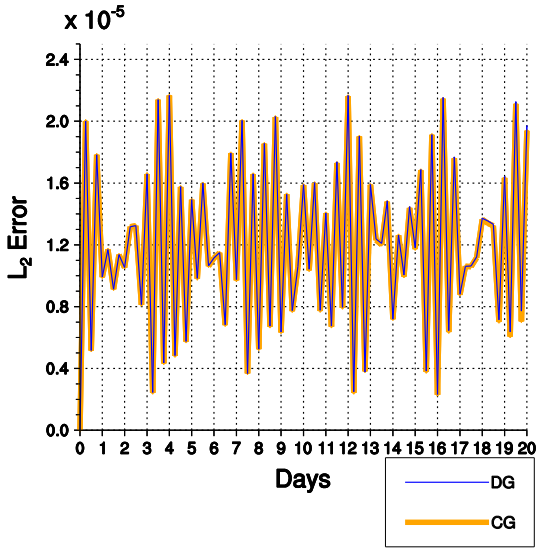

588

589 FIG. 4. L2 error norm of surface pressure in Pa for the CG and DG simulations at the

590 $H = 128$ ($n_H = 16$ and $N = 8$) horizontal resolution and 26 vertical levels.

591

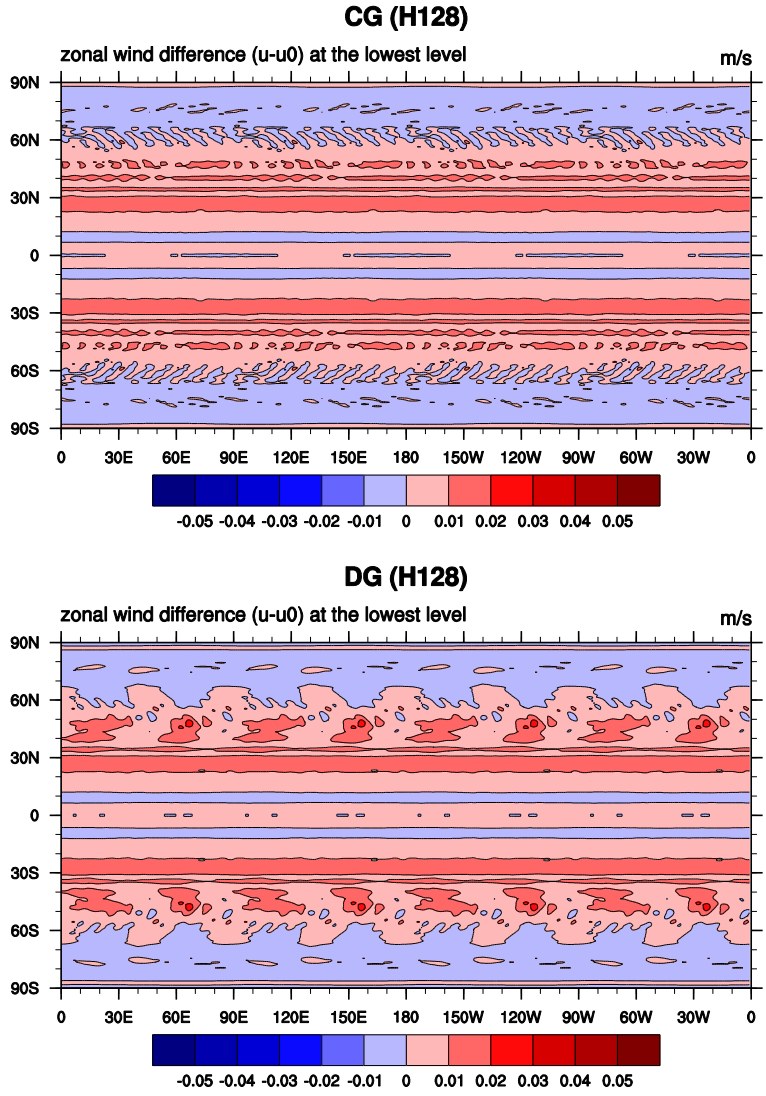

592

593 FIG. 5. Distribution of zonal wind difference at the lowest model level between day 20

594 and day 0 for the (top) CG and (bottom) DG simulations at the $H = 128$ ($n_H = 16$ and

595 $N = 8$) horizontal resolution and 26 vertical levels.

596

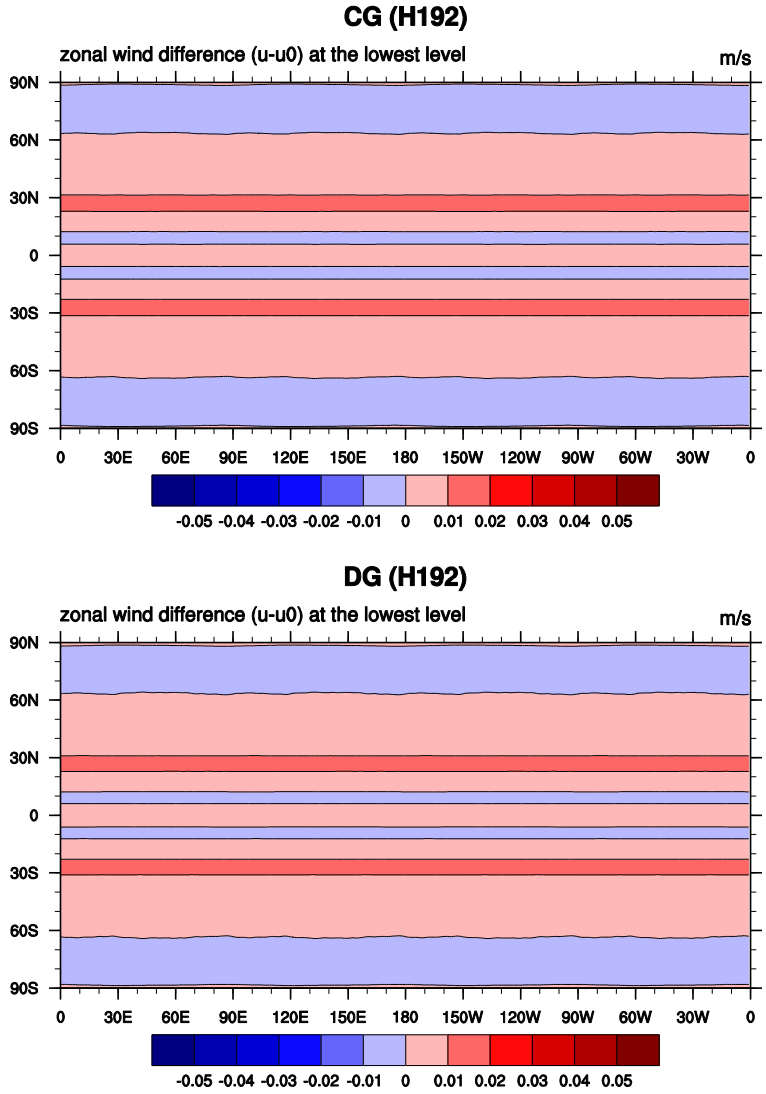

597

598 FIG. 6. As in Fig. 5 but for the $H = 192$ ($n_H = 16$ and $N = 12$) horizontal

599 resolution.

600

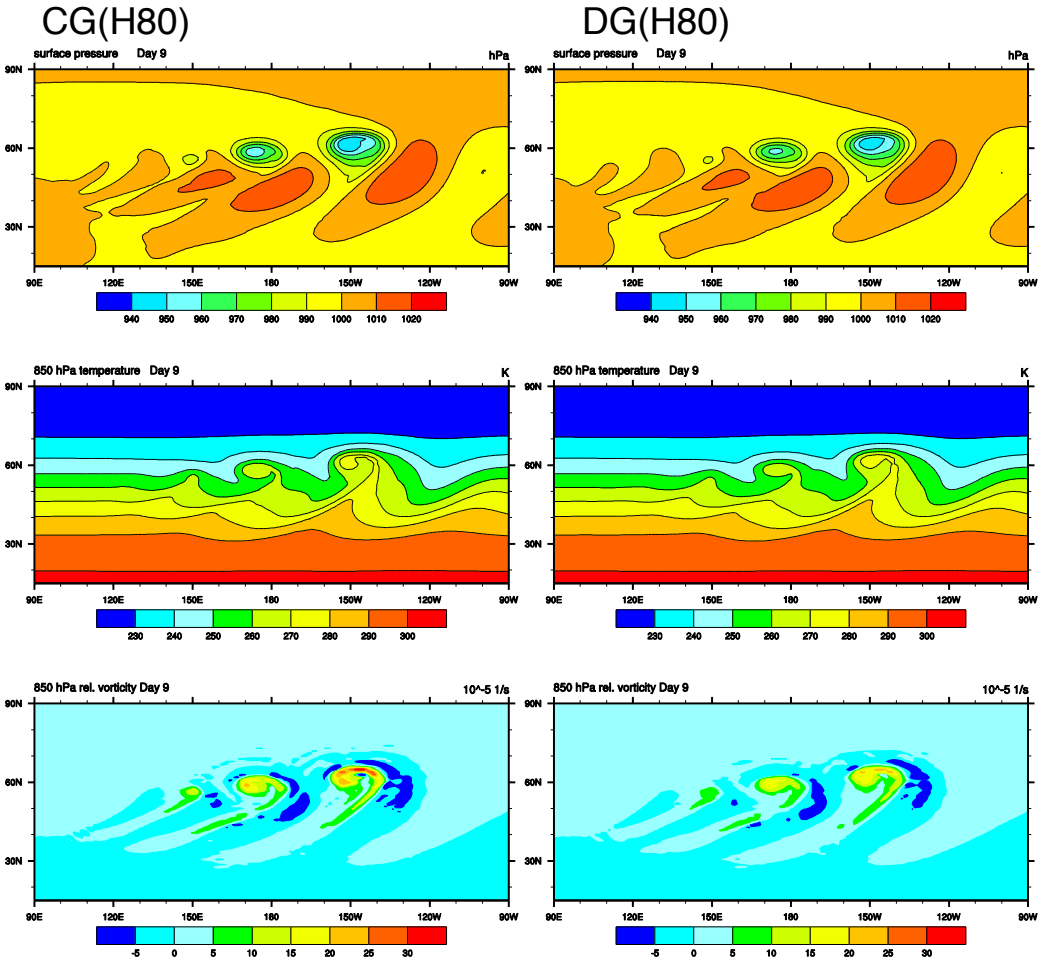

601

602 FIG. 7. Baroclinic wave at day 9 with the (left) CG and (right) DG simulations with the

603 resolution of the $H = 80$ ($n_H = 16$ and $N = 5$) horizontal resolution and 26 vertical

604 levels: (upper row) surface pressure, (middle row) 850 hPa temperature, and (bottom row)

605 850 hPa relative vorticity at days (left) 7 and (right) 9.

606

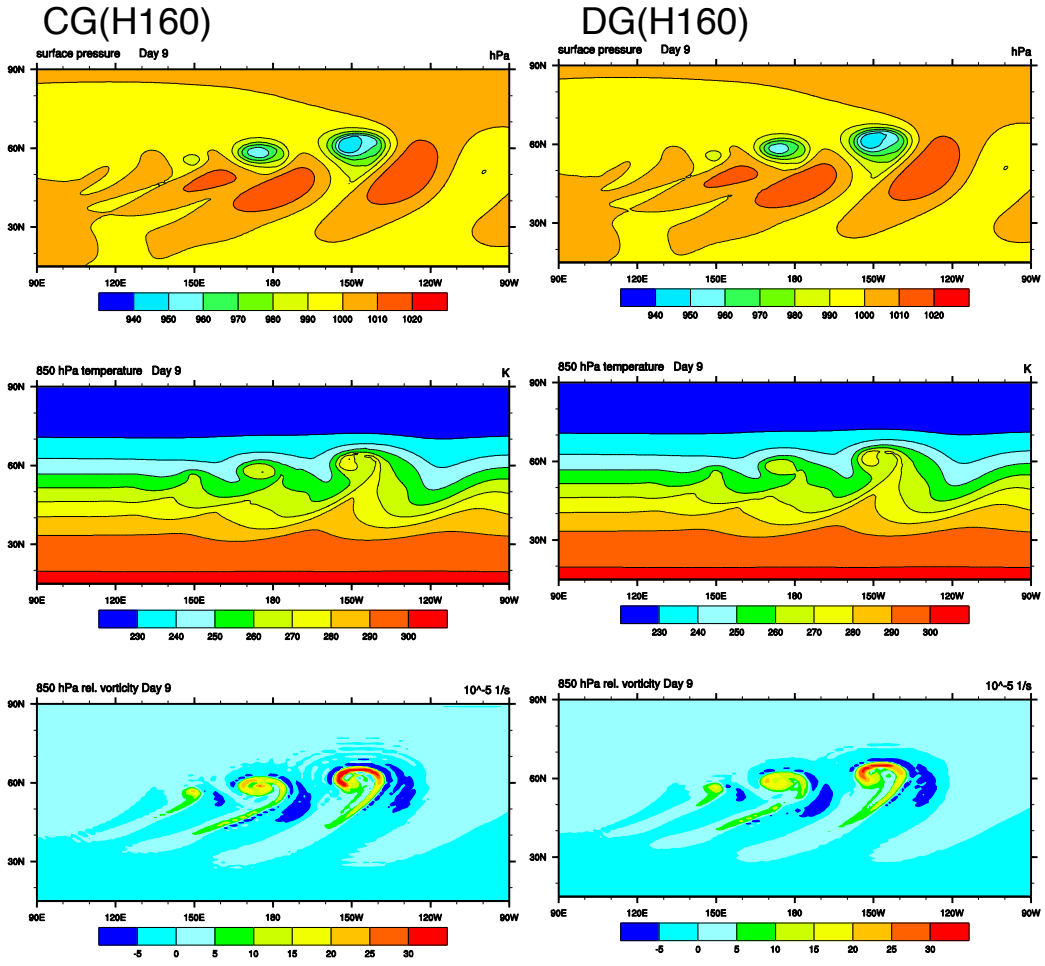

607

608 FIG. 8. As in Fig. 7 but for the $H = 160$ ($n_H = 32$ and $N = 5$).

609

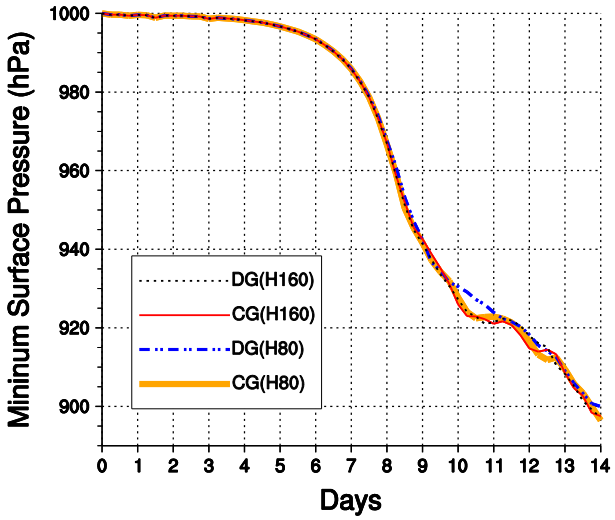

610

611 FIG. 9. The minimum surface pressure (hPa) as a function of days for the CG and DG

612 simulations with the lower resolution of the $H = 80$ ($n_H = 16$ and $N = 5$) and the higher

613 resolution of the $H = 160$ ($n_H = 32$ and $N = 5$).

614

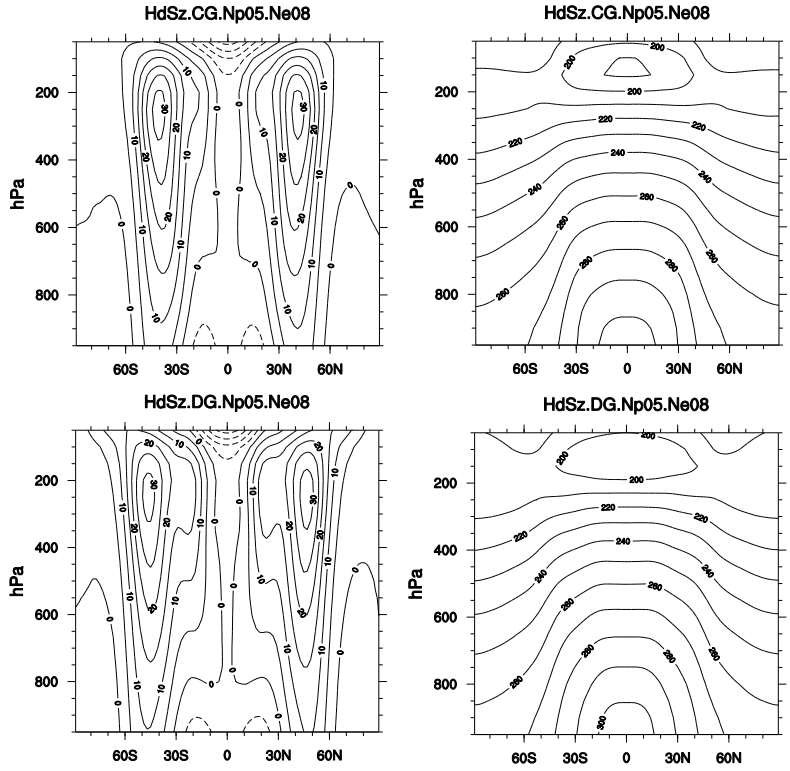

615

616 FIG. 10. The (left) mean zonally averaged zonal velocity (m/s) and (right) mean zonally
617 averaged temperature (K) for the (upper row) CG and (bottom row) DG simulations with the
618 resolution of the $H = 40$ ($n_H = 8$ and $N = 5$) and 25 vertical levels (Nlev=25). These
619 are calculated over the last 1000 days of a 1200-day integration.

620

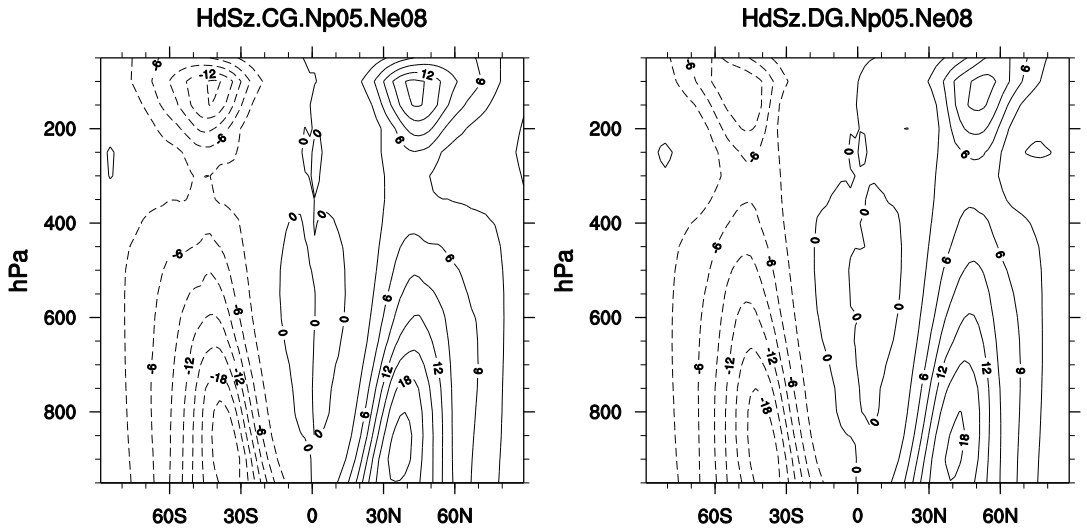

621

622 FIG. 11. The mean zonally averaged eddy heat flux for the (left) CG and (right) DG

623 simulation with the resolution of the $H = 40$ ($n_H = 8$ and $N = 5$).